ARTICLE OPEN

Check for updates

High responsivity and flexible deep-UV phototransistor based on Ta-doped β-Ga_2O_3

Xiao-Xi Li[1], Guang Zeng[1], Yu-Chun Li[1], Hao Zhang[1], Zhi-Gang Ji[2], Ying-Guo Yang[1,3]✉, Man Luo[4], Wei-Da Hu[4], David Wei Zhang[1]✉ and Hong-Liang Lu[1]✉

Deep-ultraviolet (DUV) phototransistors have shown great potential applications in UV imaging, artificial intelligence, and wearable optoelectronics. Among a large number of wide bandgap semiconductors, the quasi-two-dimensional β-Ga_2O_3 is considered as an ideal candidate for DUV photodetector applications. Herein, we report a high responsivity (R) and fully flexible Ta-doped β-Ga_2O_3 DUV phototransistor which exhibits outstanding optoelectrical properties with a high R of 1.32×10^6 A/W, a large detectivity of 5.68×10^{14} Jones, a great photo-to-dark current ratio of 1.10×10^{10}%, a high external quantum efficiency of 6.60×10^8%, and an ultra-fast response time of ~3.50 ms. Besides, the flexible Ta-doped β-Ga_2O_3 device also displays high reliability and mechanical flexibility that can sustain well after over 1×10^4 bending cycles. Moreover, high-contrast imaging of UV light was obtained on the flexible DUV detector arrays, which can be efficiently trained and recognized by an artificial neural network. Our findings offer a perspective to develop wearable optoelectronics and UV imaging based on high-performance flexible β-Ga_2O_3 DUV phototransistors, providing an inspiration for the future work in artificial intelligence and bionic robot fields.

npj Flexible Electronics (2022)6:47 ; https://doi.org/10.1038/s41528-022-00179-3

INTRODUCTION

Deep-ultraviolet (DUV) photodetectors with an advantage of directly converting UV into an electrical signal have recently attracted much attention, which play a key role in the fields of UV imaging, secure communication, biological detection, military detection, etc[1–3]. Due to the outstanding characteristics of DUV photodetectors, such as high sensitivity, fast response speed, and low dark current[4–7], various wide bandgap semiconductors (AlN, ZnO, GaN, and Ga_2O_3) have been expanded to DUV fields[8–11]. Typically, quasi-two-dimensional (2D) β-Ga_2O_3 is considered as an ideal candidate for DUV photodetector applications because of its suitable direct bandgap of ~4.90 eV, high breakdown electrical field of ~9 MV/cm, outstanding thermal stability, high adsorption coefficient, etc.[12–14]. However, the current high-performance β-Ga_2O_3-based UV photodetectors are usually fabricated on rigid substrates, which limit their applications in many novel device concepts such as transparent, wearable, and portable fields[15].

It is no doubt that photodetectors based on flexible substrates could meet the growing demands of next-generation optoelectronics with low manufacturing cost, better portability, and lightweight design. Unfortunately, little attention of recent reports has been paid on the flexible β-Ga_2O_3 DUV photodetectors to date. Sooyeoun et al. fabricated β-Ga_2O_3 photodiode with graphene electrodes based on polyethylene terephthalate substrate, exhibiting a photo-to-dark current ratio (PDCR) of $\sim 1 \times 10^6$% and a responsivity (R) of ~29.8 A/W[16]; Wang et al. reported flexible graphene/amorphous Ga_2O_3 van der Waals heterojunction with a PDCR of $\sim 1 \times 10^7$% and a R of ~22.75 A/W[17]; etc. While the performances of the presented flexible β-Ga_2O_3 DUV photodiodes, especially in terms of R, are not competitive with their rigid devices[18]. Many strategies have been recently proposed to improve the performance of flexible β-Ga_2O_3 DUV photodetectors. On one hand, better than the reported photodiodes, the phototransistors, as one kind of three-terminal photodetectors, have showed a significant advantage of the intrinsic current modulation, high intrinsic gain, and low dark current, which have been considered as an alternative solution to further improve the performance of DUV photodetectors[19]. On the other hand, for the material itself, various affordable and high-quality growth techniques for β-Ga_2O_3 bulk single crystals have been developed, including edge-defined film-fed growth, the optical floating zone (OFZ), the Czochralski, and so on[20].

Herein, the high-quality Ta-doped β-Ga_2O_3 single crystal has been grown by using an optimized OFZ method. Subsequently, a fully flexible high-performance β-Ga_2O_3 phototransistor on polyimide (PI) substrate was fabricated. The hexagonal boron nitride (h-BN) is selected as an ideal dielectric due to its large bandgap (5.97 eV), high breakdown field (8–12 MV/cm), atomically flat surface without unnecessary dangling bonds, and high thermal conductivity [1700–2000 W/(m K)][21–23]. The obtained β-Ga_2O_3 phototransistor exhibits a high R of 1.32×10^6 A/W, a large detectivity (D^*) of 5.68×10^{14} Jones, a great PDCR of 1.10×10^{10}%, a high external quantum efficiency (EQE) of 6.60×10^8%, and an ultra-fast response time of ~3.5 ms. Then, the reliability and mechanical flexibility of the fabricated β-Ga_2O_3 phototransistor were explored. Besides, as a proof-of-concept, the flexible DUV detector arrays based on the present β-Ga_2O_3 phototransistors, combining with an artificial neural network (ANN), can perform image recognition efficiently and accurately. These results show that high-performance flexible DUV β-Ga_2O_3 phototransistors have great application potential in future wearable optoelectronics, UV imaging, and artificial intelligence fields.

[1]State Key Laboratory of ASIC and System, Shanghai Institute of Intelligent Electronics & Systems, School of Microelectronics, Fudan University, 200433 Shanghai, China. [2]National Key Laboratory of Science and Technology on Micro/Nano Fabrication, Shanghai Jiao Tong University, 200240 Shanghai, China. [3]Shanghai Synchrotron Radiation Facility (SSRF), Zhangjiang Lab, Shanghai Advanced Research Institute &, Shanghai Institute of Applied Physics, Chinese Academy of Sciences, 201204 Shanghai, China. [4]State Key Laboratory of Infrared Physics, Shanghai Institute of Technical Physics, Chinese Academy of Sciences, 200083 Shanghai, China. ✉email: yangyingguo@sinap.ac.cn; dwzhang@fudan.edu.cn; honglianglu@fudan.edu.cn

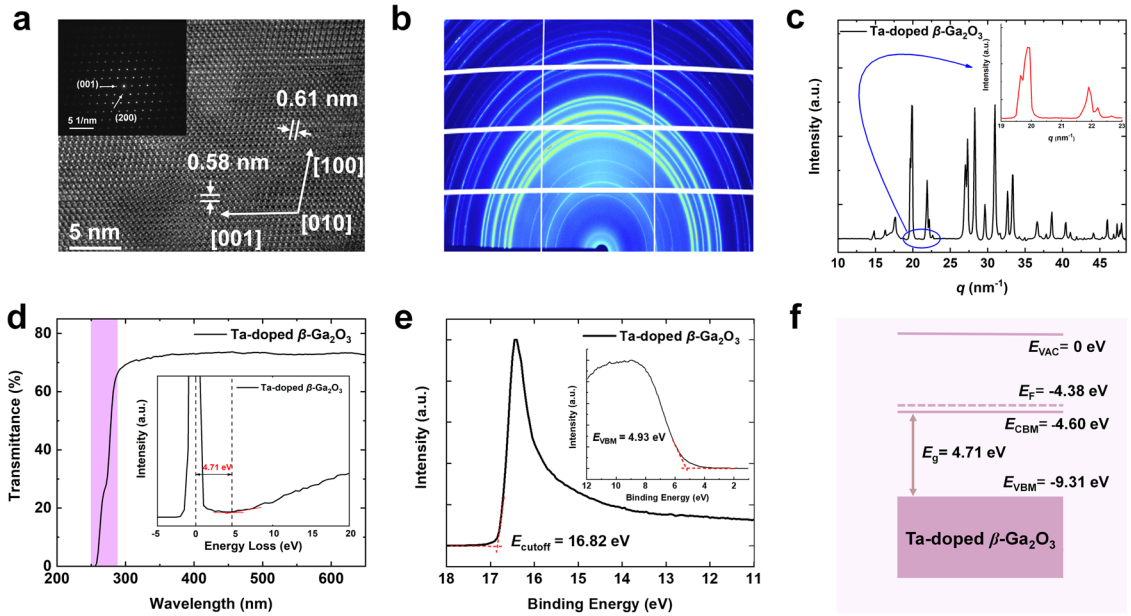

Fig. 1 Material characterizations of Ta-doped β-Ga_2O_3. **a** The HR-TEM image of the exfoliated Ta-doped β-Ga_2O_3 flake. Inset: the SAED pattern of the exfoliated Ta-doped β-Ga_2O_3 flake. **b** 2D-GIXRD pattern of the Ta-doped β-Ga_2O_3. **c** The integrated 1D-GIXRD spectrum of the Ta-doped β-Ga_2O_3. **d** The transmittance spectrum of the Ta-doped β-Ga_2O_3 bulk single crystal. Inset: the REELS spectrum of the Ta-doped β-Ga_2O_3. **e** The UPS spectra of the Ta-doped β-Ga_2O_3. **f** The energy band diagram of the Ta-doped β-Ga_2O_3.

RESULTS AND DISCUSSION

Material characterizations of Ta-doped β-Ga_2O_3

To determine the morphology and crystalline phase of the obtained Ta-doped β-Ga_2O_3 material, the high-resolution transmission electron microscopy (HR-TEM) measurement was conducted. The spacings of lattice fringe shown in Fig. 1a were calculated to be ~0.61 and ~0.58 nm for (200) and (001) atomic planes respectively, which agrees well with the results reported in the literature[24]. Notably, even with a suitable amount of Ta ion doping, there is almost no obvious lattice damage observed by the HR-TEM, indicating a good crystal quality of β-Ga_2O_3 material. The selected-area electron diffraction (SAED) pattern in the inset of Fig. 1a further confirms the perfect lattice symmetry and the lattice parameters of exfoliated β-Ga_2O_3 flakes. Synchrotron-based grazing incidence X-ray diffraction (GIXRD) measurement was used to analyze the fine crystalline structure of the β-Ga_2O_3 sample. The two-dimensional GIXRD (2D-GIXRD) pattern of Ta-doped β-Ga_2O_3 is presented in Fig. 1b, which displays the clear and bright diffraction rings. Figure 1c shows the corresponding azimuthally integrated one-dimensional GIXRD (1D-GIXRD) spectrum of Ta-doped β-Ga_2O_3, demonstrating the typical peaks of β-Ga_2O_3, which are well consistent with the standard JCPDF (41–1103)[25]. Notably, as shown in the inset figure, two diffraction peaks located at q ~21.12 nm^{-1} and 22.49 nm^{-1}, which are assigned to be (400) and (002) planes, show an obvious split in peak shape and a significant increase in peak intensity, implying the Ta^{5+} doping could effectively occupy the ion vacancies (or substitute Ga^{3+}) and thereby improve the crystalline of the parent β-Ga_2O_3[26]. Then, the optical transmittance spectrum of Ta-doped β-Ga_2O_3 bulk single crystal is analyzed in Fig. 1d. In the visible light region of 400–650 nm wavelength, the transmittance value of the current β-Ga_2O_3 bulk single crystal is ~73%. The cutoff absorption edge is located at ~260 nm. The energy band gap (E_g) of Ta-doped β-Ga_2O_3 is also determined to be 4.71 eV from reflection electron energy loss spectroscopy (REELS) in the inset of Fig. 1d. Furthermore, the ultraviolet photoelectron spectroscopy (UPS) measurement was employed to investigate the energy level alignment of Ta-doped β-Ga_2O_3. As displayed in Fig. 1e, the corresponding work function and valence band maximum (E_{VBM}) of the Ta-doped β-Ga_2O_3 are calculated to be 4.38 and 9.31 eV, respectively. Thus, the Fermi level (E_F) of the Ta-doped β-Ga_2O_3 sample is located at −4.38 eV. The E_{VBM} is located at 4.93 eV below the E_F. Combined with the E_g measured from REELS spectrum (4.71 eV for the present Ta-doped β-Ga_2O_3), the band diagram of Ta-doped β-Ga_2O_3 is summarized in Fig. 1f. Obviously, the E_F of Ta-doped β-Ga_2O_3 is above the conduction band minimum (E_{CBM}) with 0.22 eV, which would greatly contribute to increase the electron concentration[27].

Interface and electrical properties of the β-Ga_2O_3 device

Next, a Ta-doped β-Ga_2O_3 metal insulator semiconductor field effect transistor (MISFET) with h-BN dielectric was fabricated. The β-Ga_2O_3 and h-BN flakes were mechanically exfoliated and sequentially transferred onto a SiO_2/Si substrate. Firstly, the interface properties at Ta-doped β-Ga_2O_3/ h-BN heterostructure were investigated. Figure 2a shows the cross-sectional HR-TEM image of the stacked Ta-doped β-Ga_2O_3/h-BN heterostructure on the SiO_2/Si substrate. No obvious deformation or fault was observed in each layer and the interface β-Ga_2O_3/h-BN heterostructure. And from Fig. 2a it can be seen the thickness of exfoliated β-Ga_2O_3 flake is 165 nm. The HR-TEM image of an enlarged area for the interface of Ta-doped β-Ga_2O_3/h-BN heterostructure is displayed in Fig. 2b. Note that, the highly crystalline nature of the β-Ga_2O_3 and h-BN and atomically sharp interface at β-Ga_2O_3/h-BN heterostructure are evident. In addition, high-magnification cross-sectional HR-TEM images of the h-BN flake and the interface of Ta-doped β-Ga_2O_3/h-BN heterostructure were shown in Fig. 2c. The displacements of h-BN were calculated to 3.4 Å, which is consistent with the value in the literature[28]. While the ordered lattice fringe formed at the β-Ga_2O_3/h-BN interface has a spacing of 4.0 Å, which is slightly larger than that in the bulk of h-BN, which might be attributed to the excessive residual stress at the interface of β-Ga_2O_3/h-BN[29]. The corresponding energy band diagram of Ta-doped β-Ga_2O_3/h-BN heterostructure was established in Supplementary Fig. 1. It can be clearly seen that the β-Ga_2O_3/h-BN heterostructure system has a staggered band alignment (type II)[30]. The valence and conduction band offsets (ΔE_V and ΔE_C) of Ta-doped β-Ga_2O_3/h-BN

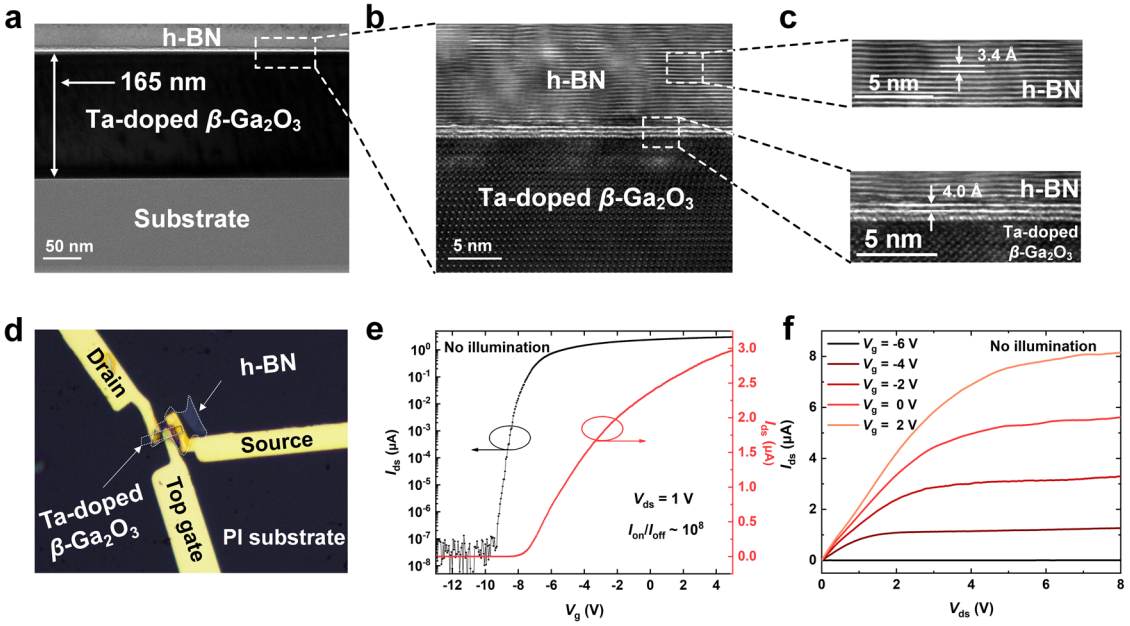

Fig. 2 Interface analysis and electrical properties of the Ta-doped β-Ga_2O_3 transistor. a Cross-sectional HR-TEM image of the stacked Ta-doped β-Ga_2O_3/h-BN heterostructure on SiO_2/Si substrate. **b** High-magnification HR-TEM image of an enlarged area for the interface of Ta-doped β-Ga_2O_3/h-BN heterostructure. **c** Top image: High-magnification cross-sectional HR-TEM image of the h-BN flake. Bottom image: high-magnification cross-sectional HR-TEM image of the interface of Ta-doped β-Ga_2O_3/h-BN heterostructure. **d** The optical microscopic image of the fabricated β-Ga_2O_3 transistor. **e** The transfer curves (I_{ds}-V_g) of the fabricated β-Ga_2O_3 transistor in log and linear scales under dark condition at $V_{ds} = 1$ V. **f** The output curves (I_{ds}-V_{ds}) of the fabricated β-Ga_2O_3 transistor.

heterostructure are 3.42 and 4.68 eV, which could provide a high sufficient barrier height to reduce electron tunneling through the interface due to quantum tunneling effect or thermal fluctuations[31]. Subsequently, to broaden applications in the emerging area such as wearable and portable electronics and optoelectronics, a flexible β-Ga_2O_3 phototransistor with h-BN dielectric was fabricated on PI substrate. The PI film was chosen as a flexible substrate due to its capability of withstanding high temperatures up to 350 °C and other advantages such as light-weight, low-cost, soft, and flat surface[32,33]. The PI substrate used here was spin-coated and cured on the glass film, which corresponds to the optical image (Supplementary Fig. 2). It can be found that the PI film shows high flexibility and foldability. Next, the optical microscopy image of the fabricated β-Ga_2O_3 transistor is shown in Fig. 2d. The length (L) and width (W) of the β-Ga_2O_3 channel are ~2.6 and ~2.5 μm in sequence. The measured thicknesses of β-Ga_2O_3 channel layer and h-BN dielectric layer by atomic force microscope (AFM) are ~199.5 and ~11.3 nm (Supplementary Fig. 3), respectively. Then, the electrical properties of the fabricated flexible β-Ga_2O_3 transistor were measured and analyzed. Figure 2e displays the transfer curves of the fabricated β-Ga_2O_3 transistor in log and linear scales under dark condition at $V_{ds} = 1$ V, which exhibits a high on/off current ratio (I_{on}/I_{off}) of ~10^8 and a low off-state current (I_{off}) of ~10 fA. The threshold voltage (V_{th}) is extracted as −8.30 V using a linear extrapolation method at $V_{ds} =$ 1 V. The transconductance (g_m) as a function of V_g is extracted using $g_m = \frac{\partial I_{ds}}{\partial V_g}$ (Supplementary Fig. 4)[34]. The maximum value of transconductance (g_{max}) can reach 0.49 μS at $V_g = -6.65$ V. The field-effect electron mobility (μ_{fe}) is also extracted using the equation of $\mu_{fe} = \frac{L}{W \times C_{ox} \times V_{ds}} \times g_m$, where L and W are the length and width of β-Ga_2O_3 channel, and C_{ox} is the capacitance of gate dielectric per unit area[34]. C_{ox} is calculated as 3.13×10^{-7} F/cm^2, using the formula of $C_{ox} = \frac{\varepsilon_0 \varepsilon_r}{d}$ where ε_0 is the vacuum permittivity (8.854×10^{-12} F/m), ε_r is the relative permittivity of h-BN (~4), and d is the dielectric thickness (11.3 nm)[34]. And the peak value of μ_{fe} is calculated to be 1.6 cm^2/V·s. Figure 2f shows the output characteristic of β-Ga_2O_3 transistor where V_g varies from −6 to 2 V with a step of 2 V. The sharp pinch-off and outstanding saturation of current can be clearly observed. These results show that β-Ga_2O_3 phototransistors have good gate tunability and electrical properties.

The photoelectrical properties of the β-Ga_2O_3 device

Subsequently the photoelectrical properties of the fabricated β-Ga_2O_3 phototransistor were investigated systematically. In general, the photocurrent generation mechanisms are mainly categorized as photoconductive (PC) and photogating (PG) effects for 2D material phototransistors[35]. In the PC effect, the absorption of photons generates extra free carriers, increasing channel current, and thus the electrical resistance of channel was reduced (Supplementary Fig. 5). While PG effect is a particular example of the PC effect. If the photogenerated holes in n-type transistor are trapped in localized states of which energy near the valence band edge, they can perform as a local gate voltage (ΔV_g), effectively modulating the electrical resistance of semiconductor channel (Supplementary Fig. 6)[36]. It is worth noting that the trapped photocarriers will prolong the lifetime of photogenerated carriers ($\tau_{photocarriers}$), usually leading to a large photoconductive gain (G)[37], as detailed in Supplementary Section S1 and Eq. (S1).

To investigate the mechanism of photocurrent generation in β-Ga_2O_3 channel, we measured I_{ds}-V_g characteristic under a series of illumination P_{in} at 250 nm excitation wavelength, as shown in Fig. 3a. The UV light source illuminates the surface of the device vertically and covers the entire channel. It is observed that the photocurrent (I_{ph}) of device increases with increasing illumination densities. Then the curves of I_{ph} as a function of V_g were plotted under different illumination P_{in} at $V_{ds} = 1$ V in Fig. 3b. Obviously, I_{ph} increases with the optical power. On one hand, this phenomenon is caused by the higher illumination P_{in} that can excite more photogenerated carriers, in turn, enhancing the PC effect. On the other hand, it is caused by trapping more photogenerated holes, increasing the PG effect mentioned above. But for a fixed power, the photocurrent accesses a maximum value. It is because that the effective modulation of V_g affects PC

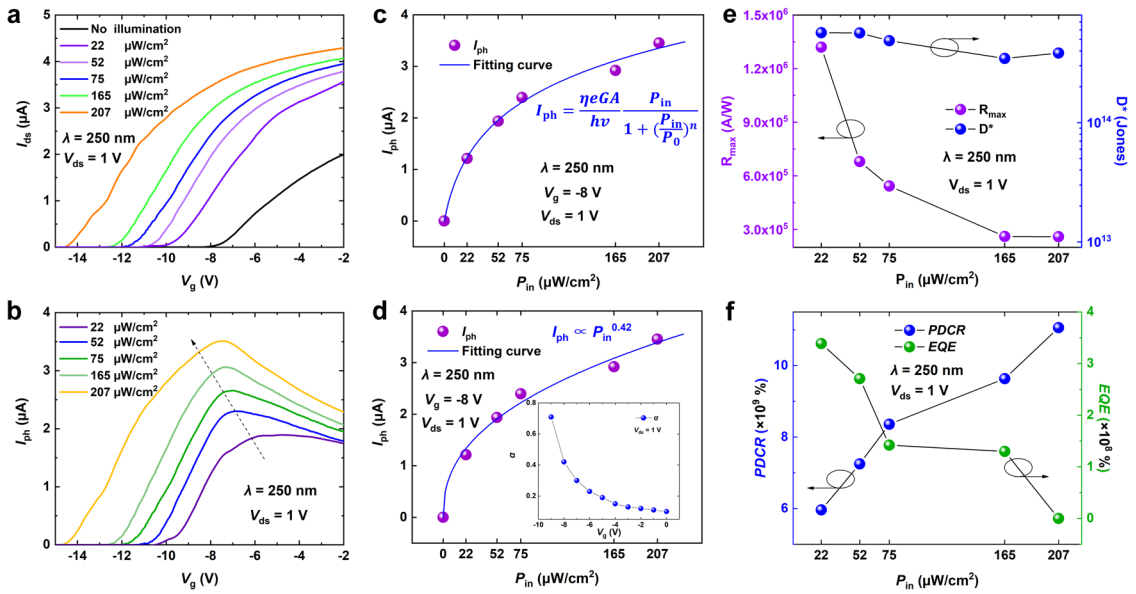

Fig. 3 The photoelectrical properties of the fabricated β-Ga_2O_3 phototransistor. At 250 nm excitation wavelength. **a** Transfer characteristic of the device under the dark and different illumination power intensities (P_{in}) conditions at $V_{ds} = 1$ V. **b** Dependence of I_{ph} on V_g under different illumination P_{in} at $V_{ds} = 1$ V. **c** The P_{in} dependence of I_{ph} curve at a fixed gate voltage of −8 V and $V_{ds} = 1$ V. **d** The I_{ph} as a function of P_{in} at $V_g = -8$ V and $V_{ds} = 1$ V. Inset: α as a function of V_g. **e** The corresponding R_{max} and D^* dependence of P_{in}. **f** PDCR and EQE values versus P_{in} at $V_{ds} = 1$ V.

and PG effects[38]. Moreover, the generated I_{ph} can be fitted successfully by the empirical Hornbeck-Haynes model (Supplementary Section S1 and Eq. (S2))[39]. The P_{in} dependence of I_{ph} curve at a fixed gate voltage of −8 V is presented in Fig. 3c. The bule line is the fitting results according to Supplementary Equation S2, from which $\eta\frac{\tau_{photocarriers}}{\tau_{transit}} = 8606$ and $n = 0.79$ have been deduced, where η is the efficiency of converting absorbed photons to electrons, $\tau_{transit}$ is the transit time of carriers, and n is a phenomenological fitting parameter[40]. According to the equation of $\tau_{transit} = \frac{L^2}{\mu_{fe}V_{ds}}$, $\tau_{transit}$ is calculated to be 42 ns where $L = 2.6$ μm, $V_{ds} = 1$ V, and $\mu_{fe} = 1.6\ cm^2/V{\cdot}s$. According to the transmittance spectrum in Fig. 1d, a reasonable absorption rate of 30% is assumed. Then the values of G and $\tau_{photocarriers}$ can be derived to be about 2.8×10^4 and 1.2 ms, respectively. And the bandwidth of a photodetector without gain decay can be roughly defined as $f_{3-dB} = \frac{1}{2\pi\tau_{photocarriers}}$. Therefore, the 3-dB bandwidth of the β-Ga_2O_3 phototransistor is calculated to be ~133 Hz. It is clearly that a larger G will cause a smaller 3-dB bandwidth due to the competing relationship between them. Then, the typical signatures of PC and PG effects are illustrated in Supplementary Section 2. Then I_{ph}-P_{in} curve at a fixed gate voltage of −8 V is extracted in Fig. 3d. The curve could be well fitted using the formula of $I_{ph} \propto P_{in}^{\alpha}$ where α is exponent. The obtained value of α is 0.42 in Fig. 3d, smaller than 1, confirming the existence of PG effect in the β-Ga_2O_3 phototransistor[41]. Subsequently, the same method was used to extract α under a series of fixed gate voltages and the α-V_g curve was plotted in the inset of Fig. 3d. It reveals that α ranges from 0.71 to 0.1 when V_g changes from −9 to 0 V, indicating that the PG effect has a V_g-dependent relation which is consistent to Supplementary Equation S3. It is also observed that V_{th} of n-type β-Ga_2O_3 device shifted in negative direction from −7.50 to −14.50 V, which can be clearly interpreted by PG effect. The dependence of the change of threshold voltage ($|\Delta V_{th}|$) on P_{in} was also extracted and plotted in Supplementary Fig. 7. The V_{th} drifts negatively with increasing P_{in}. It can be assumed that the local gate electric field formed by trapped holes effectively changes the Fermi level and generates more electrons in β-Ga_2O_3 channel, causing a stronger PG effect.

The critical parameters including R, D^*, PDCR, and EQE are extracted to further evaluate the performances of the fabricated β-Ga_2O_3 phototransistor[42]. The R of the β-Ga_2O_3 phototransistor is extracted firstly (Supplementary Fig. 8) from Fig. 3b using[43]

$$R = \frac{I_{ph}}{P_{in} \times A} \quad (1)$$

where A is the active area of the phototransistor. From Eq. (1), it can be found that the R and I_{ph} meet the linear relationship under a fixed P_{in}. Therefore, the trend of I_{ph}–V_g and R–V_g curves is the same under a fixed power density. Then the maximum response (R_{max}) was extracted from Supplementary Fig. 8 and plotted the corresponding R_{max} - P_{in} curve in Fig. 3e. This result shows R_{max} of the β-Ga_2O_3 phototransistor can reach 1.32×10^6 A/W at a low illumination density of 22 μW/cm², which is much superior to previous reported β-Ga_2O_3-based photodetectors under similar power conditions[7,44,45]. It is also noteworthy that R_{max} monotonically decreases with increasing illumination P_{in}. It is owing to the gradually filled trap states[38], which is also related to the multi-faceted generation, separation, and transport processes of photogenerated carriers[34]. In addition, D^* is another photodetector parameter which indicates the signal-to-noise ratio, shot current, considering the thermal, generation-recombination, and background radiations[46]. Assuming that the shot noise caused by dark current (I_{dark}) is the main noise source of total noise, D^* can be given by[47]

$$D^* = \frac{RA^{0.5}}{(2eI_{dark})^{0.5}} \quad (2)$$

where e is the electron charge (~1.6×10^{-19} C), as displayed in Fig. 3e. It can be seen that the D^* reaches the maximum value of 5.68×10^{14} Jones at the illumination P_{in} of 22 μW/cm² and maintains the same order of 10^{14} when a series of power changes, which is comparable to previous reported β-Ga_2O_3 photodetectors[46,48,49]. While this method neglected 1/f noise which predominates in the MISFET-based phototransistors[50]. In order to comprehensively evaluate D^*, the low frequency noise measurement is also conducted to extract the D^* which was defined as $D^* = R \times \frac{\sqrt{AB}}{i_N} = R \times \frac{\sqrt{A}}{S_n}$, where R is responsivity, A is the active area of the phototransistor in a unit

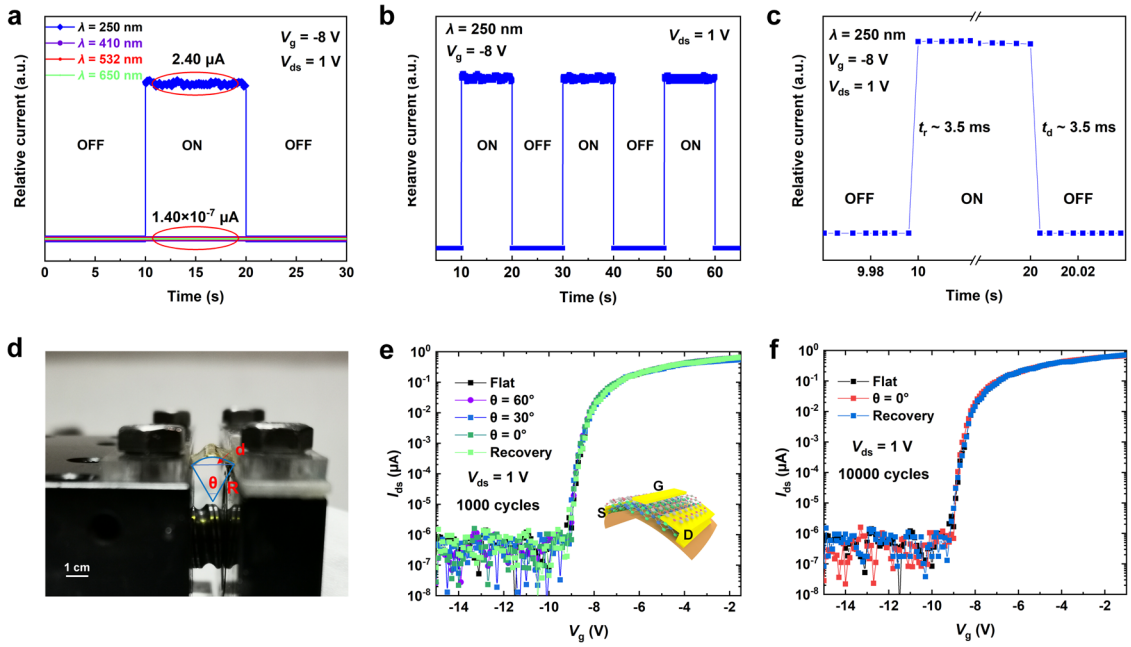

Fig. 4 The time response and stability properties of the fabricated β-Ga_2O_3 phototransistor. a Time-dependent photoresponse of β-Ga_2O_3 device under different wavelengths at $V_{ds} = 1$ V and $V_g = -8$ V. **b** Time-dependent photoresponse of β-Ga_2O_3 device under 250 nm excitation wavelength at $V_{ds} = 1$ V and $V_g = -8$ V. **c** Enlarged view of the rise and decay edges of the curve in **b**. **d** The real image of the bending state of the displayed flexible β-Ga_2O_3 device with a predefined bending angle. **e** Transfer curves of the device after the device is folded 10^3 cycles at different angles. **f** Transfer curves of the device after the device is folded 10^4 cycles at 0°.

of cm^2, B is the bandwidth, i_N is the measured noise current of the phototransistor, and S_n is the noise current density[51]. The Supplementary Fig. 9a shows that the noise power spectral density for $V_g = -8.45$, -8.00, -7.60, and -7.35 V, respectively. The Supplementary Fig. 9b shows the noise current density extracted from the Supplementary Fig. 9a at the noise frequency of 10^0, 10^1, 10^2, and 10^3 Hz. It can be found that S_n increases when the V_g increases under a fixed noise frequency condition. As shown in Supplementary Fig. 10, the extracted D^* is 6.55×10^{13} Jones for $V_g = -8.45$ V under illumination P_{in} of 22 μW/cm^2 condition, which is lower 100 times than that extracted directly using the I_{dark} method (8.65×10^{15} Jones). Note that, this value of 6.55×10^{13} Jones is still very competitive with the reported literature[46,48,49]. Then, another photodetector parameter, PDCR is given by[50]

$$\mathrm{PDCR} = \frac{I_{ph}}{I_{dark}} \times 100\% \quad (3)$$

which is used to evaluate the rejection ability for noise. Obviously, the PDCR exhibits an increasing trend with P_{in}, as shown in Fig. 3f. In order to eliminate the influence of gate voltage on PDCR, we discussed the PDCR characteristic of the device at $V_g = -10$ V. The dark current at $V_g = -10$ V is about 3.18×10^{-8} μA and the I_{ph} under different P_{in} conditions at $V_g = -10$ V has been shown in Fig. 3d. The PDCR can reach 5.96×10^9% under 22 μW/cm^{-2} and increase to 1.10×10^{10}% under 207 μW/cm^{-2}. Finally, EQE means the ratio of the number of converting absorbed photons to electrons and the total number of excitation photons, which is extracted from the equation

$$\mathrm{EQE} = \left(\frac{Rhv}{e}\right) \times 100\% \quad (4)$$

where h is Planck's constant (6.626×10^{-34} J s) and υ (=c/λ) is the frequency of incident light[48]. The EQE of the device decreases gradually with increasing P_{in} as shown in Fig. 3f. The largest EQE reaches 6.60×10^8% under 22 μW/cm^2 of P_{in}. These results indicate that the obtained β-Ga_2O_3 phototransistors have outstanding photoelectrical properties.

The time response and stability properties of the device

To further study the photoresponse properties of the β-Ga_2O_3 phototransistor, time-dependent measurements on the device under various conditions were conducted. Figure 4a shows the time-dependent properties of the β-Ga_2O_3 phototransistor under different excitation wavelength. The measurement was carried out at $V_g = -8$ V and $V_{ds} = 1$ V with the P_{in} density of 75 μW/cm^2. Then, the rejection ratio is calculated as the ratio of R under 250 nm and visible (410, 532, and 650 nm) light illumination in Fig. 4a. The parameter can show the ratio of single and specific background radiation noise under illumination conditions[47]. Very clearly, there is almost no photocurrent generation under 410, 532, and 650 nm light exposure. The current of the device is ~1.40×10^{-7} μA under the three visible light illumination while the current of the device is ~2.40 μA under 250 nm light illumination. The rejection ratio of β-Ga_2O_3 phototransistor between 250 nm/visible light could reach 1.71×10^7, which exhibits high spectral selectivity. It can be confirmed that the obtained β-Ga_2O_3 phototransistor is much more sensitive to DUV light than the visible and near-IR lights. Besides, from Fig. 4a, a quick rise of I_{ph} as soon as the 250 nm laser is turned on followed by a rapid drop back to initial values when the 250 nm laser is turned off under the chopping effect of the chopper. This implies that the β-Ga_2O_3 phototransistor can act as a sensitive UV-light-activated switch. To evaluate the repeatability and stability of the device's optical response characteristic under the excitation of 250 nm laser, time dependence I_{ph} curve was measured for several cycles in Fig. 4b. The illumination light is turned on and off at an interval of 10 s with a period of 20 s. It can be found that the ON-OFF switching behavior can be retained well. To obtain the rise time (τ_r) and decay time (τ_d), Fig. 4c shows the enlarged view of the rise and decay edges of the curve in Fig. 4b. The observed switching duration for τ_r or τ_d is calculated only to be 3.5 ms, which is much faster than the reported values of other UV photodetectors[52,53]. While according to the above statement, the response time of device can be further improved if the photogating effect is reduced because there exists a compromise between them.

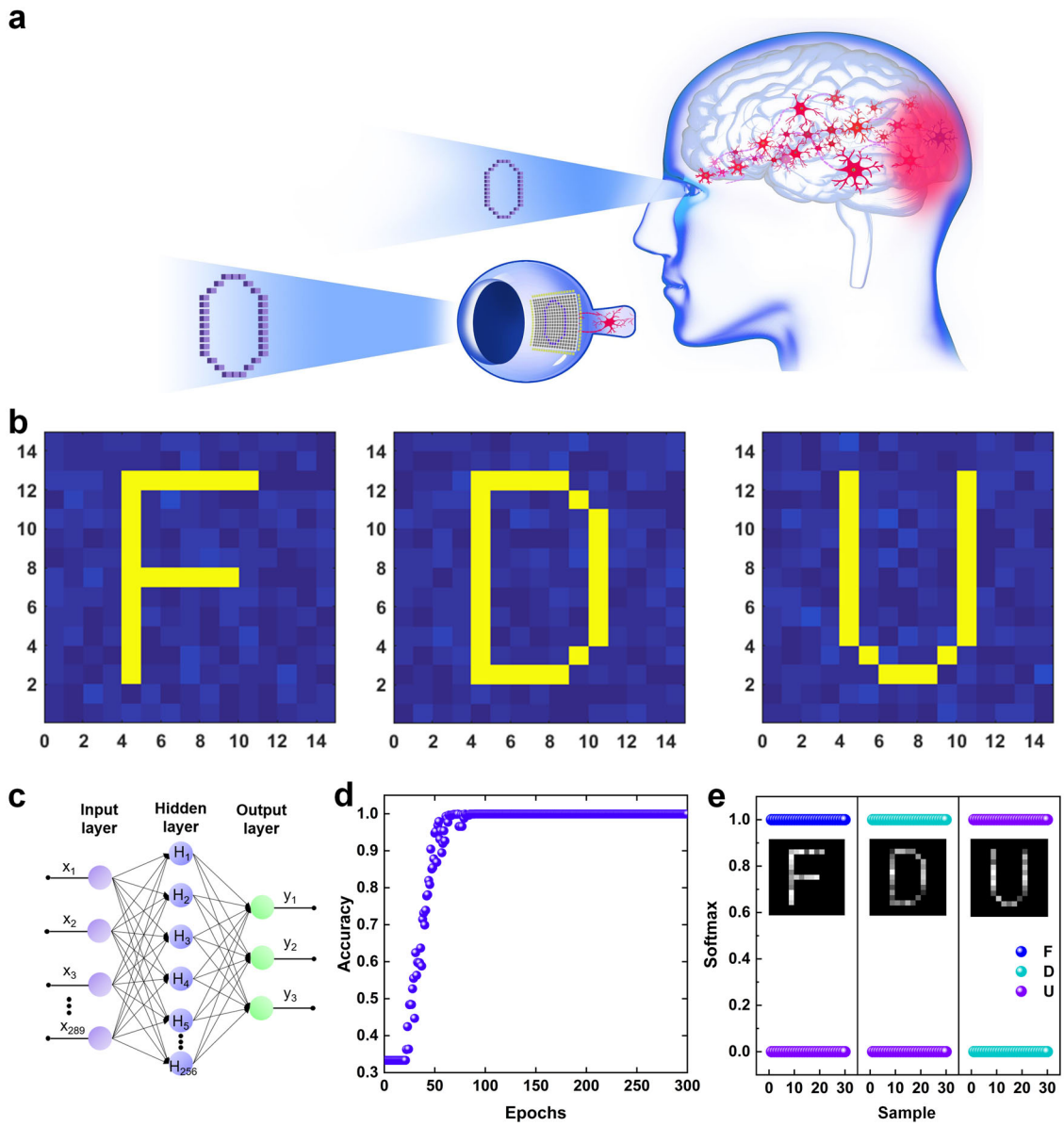

Fig. 5 The simulation of an artificial neural network (ANN) based the fabricated β-Ga_2O_3 phototransistor. a Schematic of simulating the human nerve visual system. **b** Illustration of corresponding UV detector arrays. **c** Illustration diagram of artificial visual-neural network. **d** The recognition rate of UV detector arrays recognizing image. **e** The probability for three possibility results when the letters in image database are input into the trained ANN.

Supplementary Table 1 provides a summary and comparison of key parameters for the reported UV photodetectors based on various materials. By contrast, the maximum R of β-Ga_2O_3 phototransistor (1.32×10^6 A/W) fabricated in this work is 100 times more sensitive than the traditional material photodetectors (such as GaN (10^4 A/W), SiC (0.18 A/W), ZnO (12 A/W), and others)[54–59]. In addition, the R of β-Ga_2O_3 phototransistor is also improved by more than 100 times than the reported the perovskite-based UV photodetectors (BiOBr (1.27×10^4 A/W), $Ga_2In_4S_9$ (10^4 A/W), $Sr_2Nb_3O_{10}$ (1.20×10^3), and others)[3,60–62]. Besides, Supplementary Table 2 summaries the photoresponse properties of the fabricated β-Ga_2O_3 phototransistor and compares some previous works on β-Ga_2O_3-based photodetectors. These results clearly reveal that the DUV β-Ga_2O_3 phototransistor fabricated in this work exhibits superior photoelectric performance, outperforming most reported UV photodetectors. The large responsivity stems from a strong PG effect on the β-Ga_2O_3 channel induced by the localized states in the β-Ga_2O_3 layer[6]. Finally, the reliability test of the β-Ga_2O_3 phototransistor on a flexible PI substrate was carried out. Figure 4d shows the operating platform in the experiment. We bent the device to 60°, 30°, and 0°, respectively. The transfer curves of the device after folding 10^3 times were shown in Fig. 4e. It is clear that the flexible β-Ga_2O_3 phototransistor exhibits negligible performance loss. In Fig. 4f, no performance deterioration can be observed even if the device was folded for 10^4 times at a bending angle of ~0°. It is believed that the proposed flexible β-Ga_2O_3 phototransistor has great potential in flexible UV image sensing applications due to the outstanding photosensitivity, flexibility, and stability.

An artificial neural network based on the β-Ga_2O_3 device

In recent years, the intelligent industry represented by robotics has been so flourishing that researchers are looking forward to

developing human-like bionic robots[11,63]. What's more, it also hoped that the detection range of the eyes of the bionic robot could exceed that of humans. High-performance flexible UV image sensors based on the fabricated β-Ga_2O_3 device make it possible for the robot's UV vision function. To this end, a UV detector array and an ANN are designed to artificially simulate the human vision system, as illustrated in Fig. 5a. The UV detector array composed of 15×15 pixels is designed to perceive the image. Images of the letters F, D, and U in Fig. 5b form a database used by artificial neural visual system. Obviously, images of letters formed by UV detector arrays show high contrast because the phototransistors based on β-Ga_2O_3 can produce a large I_{ph} under DUV light illumination, which makes it easier for robots to recognize and remember them. It is noted that all image signals were normalized. More detailed information is described in Supplementary Note 1. Next, a three-layer ANN was developed for training and recognizing the perceived images. As displayed in Fig. 5c, the three-layer ANN consists of input layer (225 neurons), hidden layer (128 neurons), and output layer (3 neurons). The image-recognition rate of UV detector array is illustrated in Fig. 5d. After 64 training epochs, the corresponding recognition rate could reach 0.99, which shows high image recognition efficiency. To further verify the high image recognition rate of the trained ANN, 90 image examples from above image database, including 30 "F" images, 30 "D" images, 30 "U" images, were chosen to input into the trained ANN. Then the probability for three possibility results was calculated and plotted in Fig. 5e. The results show the trained ANN has great recognition capability. As a result, the flexible UV detector array based on high-performance β-Ga_2O_3 phototransistors has a promising application in UV photosensitive imaging.

In summary, high performance and flexible DUV Ta-doped β-Ga_2O_3 phototransistor with the h-BN dielectric has been fabricated on PI substrate. The obtained Ta-doped β-Ga_2O_3 phototransistor exhibits a high R of 1.32×10^6 A/W, a large D^* of 5.68×10^{14} Jones, a great PDCR of 1.10×10^{10}%, a high EQE of 6.60×10^8%, and a fast response time of ~3.5 ms. Moreover, the flexible Ta-doped β-Ga_2O_3 device displays high reliability and mechanical flexibility that can sustain well up to 10^4 bending cycles. Furthermore, the flexible DUV detector arrays based on high-performance Ta-doped β-Ga_2O_3 phototransistors, combined with an artificial neural network, can perform image recognition efficiently and accurately. These results show high performance flexible UV Ta-doped β-Ga_2O_3 phototransistors have great potential for applications in future wearable optoelectronics, UV imaging, and artificial intelligence fields.

METHODS

Fabrication of the flexible β-Ga_2O_3 transistor

Ta-doped β-Ga_2O_3 single crystal was grown by the OFZ technique. First, the β-Ga_2O_3 (6 N) and Ta_2O_5 (4 N) powders are mixed fully by the wet ball milling and pressed into a rod by a cold isostatic press. Next, the rod was sintered in air at 1450 °C for 20 h, using <010> oriented crystal as the seed. Finally, the crystal growth starts. The obtained crystals are intact with uniform color. The schematic diagram of the fabrication method of Ta-doped β-Ga_2O_3 is illustrated in Supplementary Fig. 11.

In this study, the 0.05 mol % Ta-doped β-Ga_2O_3 singe crystal was chosen due to its suitable active carrier concentration of 1.4×10^{18} cm^{-3}. The fabrication of the flexible β-Ga_2O_3 phototransistor began by cleaning a glass substrate with isopropyl alcohol, acetone, and DI water, followed by dehydration with a nitrogen spray gun. After that, the soluble PI was deposited by spin-coating at 3000 r/min on the glass substrate and prebaked at 80 °C on a hot plate for 8 min to remove the organic solvent. Then the PI film was fully cured at 280 °C under ambient condition for 60 min. We spin-coated the soluble PI onto the glass substrate, overcoming the problem of plastic shrinkage with the high temperature processes. Next, the mechanically exfoliated β-Ga_2O_3 flake from the β-Ga_2O_3 bulk single crystal (the Raman spectrum of β-Ga_2O_3 flake is displayed in Supplementary Fig. 12) was dry-transferred to the as-fabricated PI substrate. Subsequently, Ti/Al/Ni/Au (20/100/60/80 nm) stack electrodes were deposited as source and drain contract pads via a standard electron-beam lithography, metallization, and lift-off process. The device was then annealed at 350 °C in a high-vacuum furnace with a high pure N_2 ambient for 3 h to improve ohmic contacts. Subsequently, the h-BN flake was also obtained by using the mechanical exfoliation method from a BN bulk single crystal (SixCarbon Technology Supplies) and subsequently transferred precisely onto the top of the pre-deposited β-Ga_2O_3 channel as the gate dielectric utilizing a poly (dimethylsiloxane) transfer method. Finally, the top-gate electrode of Ti/Au (10/70 nm) was patterned and deposited.

Microscopic and electrical characterizations

The active area of the phototransistor was measured to be ~2.6×2.5 μm^2 in sequence, which was characterized by the high-precision optical microscope equipment (Olympus BX53M). The high-resolution structural analysis of samples including β-Ga_2O_3 flakes, h-BN flakes, and the interface of β-Ga_2O_3/h-BN heterostructure was characterized using HR-TEM (Talos F200X). The morphology and thicknesses of β-Ga_2O_3 channel and h-BN flakes were measured by AFM (Bruker Dimension Icon). The crystalline structure of β-Ga_2O_3 samples was investigated by GIXRD which uses X-ray with a wavelength of 0.6887 Å. 2D-GIXRD pattern was obtained by a PILATUS detector at a distance of about 263 mm from the sample, and an exposure time of ~20 s. The optical transmittance characterization of β-Ga_2O_3 samples was investigated by UV-visible spectrophotometer (UV-3100). The UPS spectrum was acquired using a SPECS PHOIBOS 100 hemispherical analyzer, which was excited by an unfiltered He I (21.20 eV) gas discharge lamp. The electrical and optoelectronic properties of the β-Ga_2O_3 photodetector were measured with a semiconductor analyzer (Agilent B1500A). The UV source was provided by a deuterium lamp (THORLABS SLS204). Deuterium lamp irradiates directly the device surface through the optical fiber. The optical fiber illuminates the surface of the device vertically and covers the entire β-Ga_2O_3 channel. The response time was measured by using a chopper (C-995). The calibration of the incident power density is used by an optical power meter (THORLABS S120VC).

DATA AVAILABILITY

The data that support the findings of this study are available from the corresponding authors upon reasonable request.

Received: 14 February 2022; Accepted: 27 May 2022;
Published online: 17 June 2022

REFERENCES

1. Wang, D. et al. Bidirectional photocurrent in p-n heterojunction nanowires. *Nat. Electron.* **4**, 645–652 (2021).
2. Guo, F. et al. A nanocomposite ultraviolet photodetector based on interfacial trap-controlled charge injection. *Nat. Nanotechnol.* **7**, 798–802 (2012).
3. Gong, C. et al. Large-scale ultrathin 2D wide-bandgap BiOBr nanoflakes for gate-controlled deep-ultraviolet phototransistors. *Adv. Mater.* **32**, e1908242 (2020).
4. Hou, X. et al. High-performance harsh-environment-resistant GaO_X solar-blind photodetectors via defect and doping engineering. *Adv. Mater.* **34**, 2106923 (2022).
5. Zheng, W., Huang, F., Zheng, R. & Wu, H. Low-dimensional structure vacuum-ultraviolet-sensitive (λ < 200 nm) photodetector with fast-response speed based on high-quality AlN micro/nanowire. *Adv. Mater.* **27**, 3921–3927 (2015).
6. Qin, Y. et al. Ultra-high performance amorphous Ga_2O_3 photodetector arrays for solar-blind imaging. *Adv. Sci.* **8**, 2101106 (2021).
7. Ahn, J. et al. Ultrahigh deep-ultraviolet responsivity of a β-Ga_2O_3/MgO heterostructure-based phototransistor. *ACS Photonics* **8**, 557–566 (2021).
8. Lee, M. et al. Accelerated learning in wide-band-gap AlN artificial photonic synaptic devices: impact on suppressed shallow trap level. *Nano Lett.* **21**, 7879–7886 (2021).
9. Li, H. et al. Controllable heterogeneous nucleation for patterning high-quality vertical and horizontal ZnO microstructures toward photodetectors. *Small* **16**, 2004136 (2020).
10. Dubey, A. et al. Aluminum plasmonics enriched ultraviolet GaN photodetector with ultrahigh responsivity, detectivity, and broad bandwidth. *Adv. Sci.* **7**, 2002274 (2020).
11. Wang, T., Liang, H., Han, Z., Sui, Y. & Mei, Z. Integrated flexible Ga_2O_3 deep UV photodetectors powered by environmental electromagnetic radiation energy. *Adv. Mater.* **6**, 2000945 (2021).
12. Huang, H. et al. High aspect ratio β-Ga_2O_3 fin arrays with low-interface charge density by inverse metal-assisted chemical etching. *ACS Nano* **13**, 8784–8792 (2019).

13. Alonso-Orts, M. et al. Wide dynamic range thermometer based on luminescent optical cavities in Ga_2O_3: Cr Nanowires. *Small* **18**, 2105355 (2022).
14. Chen, T. et al. Self-powered and spectrally distinctive nanoporous Ga_2O_3/GaN epitaxial heterojunction UV photodetectors. *Adv. Photonics Res.* **2**, 2100049 (2021).
15. Kim, S. & Kim, J. Highly selective ozone-treated β-Ga_2O_3 solar-blind deep-UV photodetectors. *Appl. Phys. Lett.* **117**, 261101 (2020).
16. Oh, S., Kim, C. K. & Kim, J. High responsivity β-Ga_2O_3 metal-semiconductor-metal solar-blind photodetectors with ultraviolet transparent graphene electrodes. *ACS Photonics* **5**, 1123–1128 (2017).
17. Wang, Y. et al. Ultrasensitive flexible solar-blind photodetectors based on graphene/amorphous Ga_2O_3 van der Waals heterojunctions. *ACS Appl. Mater. Interfaces* **12**, 47714–47720 (2020).
18. Yu, S. et al. High-detectivity β-Ga_2O_3 microflake solar-blind phototransistor for weak light detection. *IEEE Electron Device Lett.* **42**, 383–386 (2021).
19. Han, Z. et al. Boosted UV photodetection performance in chemically etched amorphous Ga_2O_3 thin-film transistors. *Adv. Opt. Mater.* **8**, 201901833 (2020).
20. Zhang, J., Shi, J., Qi, D. C., Chen, L. & Zhang, H. L. Recent progress on the electronic structure, defect, and doping properties of Ga_2O_3. *APL Mater.* **8**, 020906 (2020).
21. Bae, J., Kim, H. W., Kang, I. H., Yang, G. & Kim, J. High breakdown voltage quasi-two-dimensional β-Ga_2O_3 field-effect transistors with a boron nitride field plate. *Appl. Phys. Lett.* **112**, 122102 (2018).
22. Li, X. X. et al. Effective suppression of MIS interface defects using boron nitride towards high-performance Ta-doped-β-Ga_2O_3 MISFETs. *J. Phys. Chem. Lett.* **13**, 3377–3381 (2022).
23. Watanabe, K., Taniguchi, T. & Kanda, H. Direct-bandgap properties and evidence for ultraviolet lasing of hexagonal boron nitride single crystal. *Nat. Mater.* **3**, 404–409 (2004).
24. Ahn, S. et al. Effect of front and back gates on β-Ga_2O_3 nano-belt field-effect transistors. *Appl. Phys. Lett.* **109**, 062102 (2016).
25. Zhang, J. et al. Growth and characterization of new transparent conductive oxides single crystals β-Ga_2O_3: Sn. *J. Phys. Chem. Solids* **67**, 1656–1659 (2006).
26. Wang, D., Ma, X., Xiao, H., Le, Y. & Ma, J. Ta-doped epitaxial β-Ga_2O_3 films deposited on $SrTiO_3$(100) substrates by MOCVD. *Mater. Sci. Semicond. Process* **128**, 105749 (2021).
27. Leedy, K. D. et al. Highly conductive homoepitaxial Si-doped Ga_2O_3 films on (010) β-Ga_2O_3 by pulsed laser deposition. *Appl. Phys. Lett.* **111**, 012103 (2017).
28. Gao, L., Jin, X., Li, J., Li, Y. & Sun, J. BN/Si_3N_4 nanocomposite with high strength and good machinability. *Mater. Sci. Eng. A* **415**, 145–148 (2006).
29. Sun, H. et al. Valence and conduction band offsets of β-Ga_2O_3/AlN heterojunction. *Appl. Phys. Lett.* **111**, 162105 (2017).
30. Zheng, W. et al. Direct vapor growth of 2D vertical heterostructures with tunable band alignments and interfacial charge transfer behaviors. *Adv. Sci.* **6**, 1802204 (2019).
31. Zhang, K. et al. Interlayer transition and infrared photodetection in atomically thin type-II $MoTe_2$/MoS_2 van der Waals heterostructures. *ACS Nano* **10**, 3852–3858 (2016).
32. Isaacson, S. G. et al. Fundamental limits of material toughening in molecularly confined polymers. *Nat. Mater.* **15**, 294–298 (2016).
33. Chen, Z. H., Fang, R., Li, W. & Guan, J. Stretchable transparent conductors: from micro/macromechanics to applications. *Adv. Mater.* **31**, 1900756 (2019).
34. Das, S., Chen, H., Penumatcha, A. & Appenzeller, J. High performance multilayer MoS_2 transistors with scandium contacts. *Nano Lett.* **13**, 100–105 (2013).
35. Yu, X. et al. Atomically thin noble metal dichalcogenide: a broadband mid-infrared semiconductor. *Nat. Commun.* **9**, 1545 (2018).
36. Zhao, Q. et al. The role of traps in the photocurrent generation mechanism in thin InSe photodetectors. *Mater. Horiz.* **7**, 252–262 (2020).
37. Buscema, M. et al. Photocurrent generation with two-dimensional van der Waals semiconductors. *Chem. Soc. Rev.* **44**, 3691–3718 (2015).
38. Fang, H. & Hu, W. Photogating in low dimensional photodetectors. *Adv. Sci.* **4**, 1700323 (2017).
39. Soci, C. et al. ZnO nanowire UV photodetectors with high internal gain. *Nano Lett.* **7**, 1003–1009 (2007).
40. Pradhan, B., Das, S., Li, J., Chowdhury, F. & Thomas, J. Ultrasensitive and ultrathin phototransistors and photonic synapses using perovskite quantum dots grown from graphene lattice. *Sci. Adv.* **6**, eaay5225 (2020).
41. Island, J. O., Blanter, S. I., Buscema, M., van der Zant, H. S. & Castellanos-Gomez, A. Gate controlled photocurrent generation mechanisms in high-gain In_2Se_3 phototransistors. *Nano Lett.* **15**, 7853–7858 (2015).
42. Liu, Y. et al. Ga_2O_3 field-effect-transistor-based solar-blind photodetector with fast response and high photo-to-dark current ratio. *IEEE Electron Device Lett.* **39**, 1696–1699 (2018).
43. Zhang, X. et al. High-performance beta-Ga_2O_3 thickness dependent solar blind photodetector. *Opt. Express* **28**, 4169–4177 (2020).
44. Liang, H. et al. Flexible x-ray detectors based on amorphous Ga_2O_3 thin films. *ACS Photonics* **6**, 351–359 (2018).
45. Heinze, S. et al. Carbon nanotubes as Schottky barrier transistors. *Phys. Rev. Lett.* **89**, 106801 (2002).
46. Zhao, B. et al. Solar-blind avalanche photodetector based on single ZnO-Ga_2O_3 core-shell microwire. *Nano Lett.* **15**, 3988–3993 (2015).
47. Qiu, Q. & Huang, Z. Photodetectors of 2D materials from ultraviolet to terahertz waves. *Adv. Mater.* **33**, 2008126 (2021).
48. Xu, Y. et al. Fast speed Ga_2O_3 solar-blind Schottky photodiodes with large sensitive area. *IEEE Electron Device Lett.* **41**, 997–1000 (2020).
49. Wang, Y. et al. p-GaSe/n-Ga_2O_3 van der Waals heterostructure photodetector at solar-blind wavelengths with ultrahigh responsivity and detectivity. *ACS Photonics* **8**, 2256–2264 (2021).
50. Liao, F. et al. A dual-gate MoS_2 photodetector based on interface coupling effect. *Small* **16**, 1904369 (2020).
51. Kufer, D. & Konstantatos, G. Highly sensitive, encapsulated MoS_2 photodetector with gate controllable gain and speed. *Nano Lett.* **15**, 7307–7313 (2015).
52. Zhang, Y. Y. et al. High performance flexible visible-blind ultraviolet photodetectors with two-dimensional electron gas based on unconventional release strategy. *ACS Nano* **15**, 8386–8396 (2021).
53. Moudgil, A., Sharma, K. K. & Das, S. In_2O_3/TiO_2 heterostructure for highly responsive low-noise ultraviolet photodetector. *IEEE Electron Device Lett.* **67**, 166–172 (2020).
54. Liu, L. et al. High-detectivity ultraviolet photodetectors based on laterally mesoporous GaN. *Nanoscale* **9**, 8142 (2017).
55. Aldalbahi, A. et al. A new approach for fabrications of SiC based photodetectors. *Sci. Rep.* **6**, 23457 (2016).
56. Nasiri, N., Bo, R., Wang, F., Fu, L. & Tricoli, A. Ultraporous electron-depleted ZnO nanoparticle networks for highly sensitive portable visible-blind UV photodetectors. *Adv. Mater.* **27**, 4336–4343 (2015).
57. Xu, J. et al. Efficiency enhancement of TiO_2 self-powered UV photodetectors using a transparent Ag nanowire electrode. *J. Mater. Chem. C* **6**, 3334–3340 (2018).
58. Zhu, Y. et al. Novel ultraviolet photodetector with ultrahigh photosensitivity employing SILAR-deposited ZnS film on MgZnO. *J. Alloy. Compd.* **832**, 155022 (2020).
59. Wu, J. et al. Colossal ultraviolet photoresponsivity of few-layer black phosphorus. *ACS Nano* **9**, 8070–8077 (2015).
60. Wang, F. et al. Liquid-alloy-assisted growth of 2D ternary $Ga_2In_4S_9$ toward high-performance UV photodetection. *Adv. Mater.* **31**, 1806306 (2019).
61. Li, S., Zhang, Y., Yang, W., Liu, H. & Fang, X. 2D Perovskite $Sr_2Nb_3O_{10}$ for high-performance UV photodetectors. *Adv. Mater.* **32**, 1905443 (2020).
62. Zhang, Y. et al. High-performance two-dimensional perovskite $Ca_2Nb_3O_{10}$ UV photodetectors. *Nano Lett.* **21**, 382–388 (2021).
63. Long, M., Wang, P., Fang, H. & Hu, W. Progress, challenges, and opportunities for 2D material based photodetectors. *Adv. Funct. Mater.* **29**, 1803807 (2019).

ACKNOWLEDGEMENTS

This work was supported by the National Natural Science Foundation of China (Nos. 62027818, 61874034, 12175298, and 51861135105), and Natural Science Foundation of Shanghai (Nos. 18ZR1405000 and 20ZR1464100). The authors thank beamlines BL17B1, BL19U1, and BL01B1 staff at the SSRF and User Experiment Assist System of SSRF for their help. The authors thank Professor Chang-Tai Xia's group from Key Laboratory of Materials for High Power Laser Shanghai Institute of Optics and Fine Mechanics, Chinese Academy of Sciences, for providing the β-Ga_2O_3 bulk single crystal. And Chang-Tai Xia also acknowledges the National Natural Science Foundation of China (No. 51972319) and the Science and Technology Commission of Shanghai Municipality (No. 19520744400).

AUTHOR CONTRIBUTIONS

X.X.L. fabricated the device, measured the optoelectronic properties of the photodetector and analyzed the data. G.Z., Y.C.L., and M.L. assisted with device optimization and data analysis. H.Z., W.D.H., Z.G.J., and Y.G.Y. discussed the results. X.X.L. wrote the manuscript, and all authors reviewed it. H.L.L., Y.G.Y., and D.W.Z. conceived and supervised the project.

COMPETING INTERESTS

The authors declare no competing interests.

ADDITIONAL INFORMATION

Supplementary information The online version contains supplementary material available at https://doi.org/10.1038/s41528-022-00179-3.

Correspondence and requests for materials should be addressed to Ying-Guo Yang, David Wei Zhang or Hong-Liang Lu.

Reprints and permission information is available at http://www.nature.com/reprints

Publisher's note Springer Nature remains neutral with regard to jurisdictional claims in published maps and institutional affiliations.

Open Access This article is licensed under a Creative Commons Attribution 4.0 International License, which permits use, sharing, adaptation, distribution and reproduction in any medium or format, as long as you give appropriate credit to the original author(s) and the source, provide a link to the Creative Commons license, and indicate if changes were made. The images or other third party material in this article are included in the article's Creative Commons license, unless indicated otherwise in a credit line to the material. If material is not included in the article's Creative Commons license and your intended use is not permitted by statutory regulation or exceeds the permitted use, you will need to obtain permission directly from the copyright holder. To view a copy of this license, visit http://creativecommons.org/licenses/by/4.0/.

© The Author(s) 2022